Indonesian Journal of Electrical Engineering and Informatics (IJEEI)
Vol. 12, No. 1, March 2024, pp. 125~141
ISSN: 2089-3272, DOI: 10.52549/ijeei.v12i1.4674

Enhancing Indoor Radio Tomographic Imaging Based on Normal Distribution of Sigma to Reduce RF Nodes

M. S. M. Abdullah[1], M. H. F. Rahiman[2], N. S. Khalid[3], A. S. A. Nasir[4]
[1,2,3,4]Faculty of Electrical Engineering Technology, Universiti Malaysia Perlis, Pauh Putra Campus, 02600 Arau, Perlis, Malaysia
[1,2]Centre of Excellence for Advanced Sensor Technology (CEASTech), Universiti Malaysia Perlis, Pauh Putra Campus, 02600 Arau, Perlis, Malaysia. Tel: 604-9885166, Fax: 604-988 5167

Article Info

Article history:

Received Apr 8, 2023
Revised Dec 14, 2023
Accepted Dec 27, 2023

Keyword:

Aerial Images
Caption Generation
Description Generation
Remote Sensing Images
Satellite Images

ABSTRACT

Uses the attenuation on the links between transceivers to produce an image using Radio Tomographic Imaging (RTI), a network of transceivers, or a Wireless Sensor Network (WSN). Several RTI setups have been constructed as monitoring areas. However, it is observed that most setups have limitations in the number of RF nodes due to a limited number of measurements. However, it is well known that the main difficulty in radio tomographic imaging attributes to the uncertainties in the RSS measurements of transceivers due to multipath effects, especially, when the environment of interest is much cluttered, and requirements on the larger number of nodes for the performance improvement. It is highly remarkable that the motivation of using fewer nodes in this work is to reduce the deployment cost of radio tomographic imaging, slower data collection rates, longer imaging reconstruction times, and bigger sensitivity matricest, this lead author to proposed to design and development of an RTI system with a minimum of 8 RF nodes. The strong and weak received signal strength (RSS) exhibited in the images will be used to assess the effectiveness and accuracy of human sensing localization in a region. The images were reconstructed based on selected image reconstruction algorithms, and they are Linear Back-Projection (LBP), Filtered Back Projection (FBP), Gaussian, Newton's One-step's Error Reconstruction (NOSER) and Tikhonov Regularization (TR). The reconstructed images will be analysed using the Mean Structural Similarity (MSSIM) index. A comparison between the algorithms mentioned RTI system based on the MSSIM index. NOSER and TR algorithms scored the highest for the MSSIM index overall experiments, and it is the best technique to produce images that appear similar to the original images.

Corresponding Author:

M. H. F. Rahiman,
Faculty of Electrical Engineering Technology,
Universiti Malaysia Perlis,
Pauh Putra Campus, 02600 Arau, Perlis, Malaysia
Email: hafiz@unimap.edu.my

1. INTRODUCTION

An image can be best understood by its caption. Images can be taken from front, side or top. An aerial In radio tomographic imaging, the attenuation of the connections between transceivers is estimated and used to create an image. An object obstructing the Line of Sight (LOS) between two devices will cause signal attenuation, as an image represents. By monitoring the RSS between transceiver pairs, the raw RSS data may be utilised to locate and track obstructions inside the WSN. To be classified as device-free, passive localization, this method does not need the use of a device of any kind. It is also known as device-free localization [1]–[6]. Optical cameras are the most often employed technology in DFL systems nowadays [7],

Thermal cameras, Passive Infrared (PIR) sensors [8], acoustic and vibration sensors, Ultrasound, Carbon Dioxide Based Occupancy Detection, and Radio Frequency methods [9] are all examples of passive infrared (PIR) sensors.

2. RELATED WORK

Most of the research presented in the area of RTI has focuses on single target localization and tracking. However, the RTI systems in real-world indoor and outdoor situations generally demand the localisation and tracking of a single target, where targets have crossing trajectories. As a result, numerous ongoing investigations are being undertaken to improve the RTI system's performance in terms of target localisation and precision. All studies used more than 20 RF nodes to have a perfect image, as shown in Table 1, so this paper has pushed of 8 RTI nodes to cover area monitoring for targets localization with less cost and to be set as a base for further study in future.

Table 1. Number of nodes used in RTI research areas

Work	Environment	Area	No of nodes	Technique	Algorithm	Accuracy
Chiu & Dujovn [10]	outdoor	6 m^2	12 and 24	Area error	-	0.12
Xu et al. [11]	indoor	11.52 m^2	12	RMS	Tikhonov	0.0886
					LASSO	0.1282
Piumwardane et al.[12]	outdoor	12.8m^2	12	-	-	-
Smallbon et al.[13]	indoor	25m^2	12	-	-	-
Z. Wang et al.,[14]	indoor	25m^2	16	RMSE	SubVRTI	0.52
					KRTI	0.43
					STRI	0.41
					ESRTI	0.23
Lu et al.,[15]	Indoor and outdoor	37..5m^2	20	Area error	-	0.7
Tan et al.[16]	Indoor and outdoor	24m^2	20	MSE	Tikhonov	0.338
					BCS	0.476
					HBCS	0.463
					LRSD	0.262
Q. Wang et al.[17]	Indoor	25m^2	20	Area error	VB-GMM	0.58
A. Mishra et al.[18]	Simulation	49 m^2	24	RMSE	ν-SVR	-12.83
				PAR		46.11
				SS IM		0.7931
				FSIM		0.9162
Wilson & Patwari [19]	Indoor	6.4m^2	28	MSE	Tikhonov	0.036
Bocca et al.[20]	Indoor	56m^2	33	Area error	-	0.23
Y. Zhao et al.[21]	Indoor	100m^2	34	RMSE	VRTI	0.70
					SubVRT	0.65
					KRTI	0.73
Wilson & Patwari [22]	indoor	72 m^2	34	CDF	skew-Laplace distribution	0.58
Thouin et al.[23]	Outdoor	9, 49 and 100 m^2	12, 28 and 40	OSPA	Additive Likelihood Moment	0.49
Bocca, Kaltiokallio, et al.[24]	Indoor	70, 58, and 67 m^2	30, 33 and 32	RMSE	-	0.45, 0.46 and 0.55
Sabek et al.[25]	Indoor	114 and 130 m^2	25	-		-
Proposed study	Indoor	4m^2	8	MSSIM	LBP FBP GAUSSIAN NOSER TR	0.44 0.45 0.50 0.51 0.51

As the average inaccuracy surpasses its projected performance, this research analyses the boundaries of the mathematical model and the needed parameters for RTI. Mathematical models are explained in sections III. IV and V, while system models are described. Object tracking techniques are explained in section VI. Methods and parameters are compared regarding their relative merits and demerits explained in section VII. In Section VIII, the empirical findings from an indoor setting are presented. Several model parameters are run on the same online data to determine the relative error. Section IX concludes this work.

3. MATHEMATICAL MODEL

Models for the environment and RSS for a specific connection are necessary for localization actually to occur. The system is described generally using a linear and non-linear model in these approaches, allowing for a consistent method in the estimate. The issue is unusual in the RTI systems depend on ill-posed inverses, which need approaches such as FBP, which is linear and Tikhonov Regularization, which is non-linear, used to prevent tiny noise variations from overpowering any signal data during inversion, as detailed in [1], [21], [26][27].

A. Linear model Formulation

Wilson and Patwari's linear formulation, whose methodology and general approach may also be found in [5], [7], [19], [21], [28]–[31], is one of the most often used RTI models in the literature. As seen in [19], the RSS of a particular link, i may be mathematically expressed by:

$$y_i(t) = P_i - L_i - S_i(t) - F_i(t) - v_i(t) \quad (1)$$

Where P_i is the transmitted power, static loss (loss due to distance or device characteristics) is expressed as L_i , $S_i(t)$ is the shadowing loss or loss due to objects attenuating the signal, whereas fading loss (loss due to interference in the presence of many paths) is expressed as $F_i(t)$ and $v_i(t)$ is measurement noise, all of these losses are expressed in decibels. The essential element in the linear formulation is $Si(t_c)$ which is defined as [19]:

$$S_i(t) = \sum_{j=1}^{N} w_{ij} x_j(t) \quad (2)$$

Where w_{ij} is the weight a measure of the impact link *i* has on pixel *j and* $x_j(t)$ is the attenuation in pixel *j* at time *t.* This necessitates a calibration time with an empty scene, which is a contextual as well as logistical problem when implementing an RTI system that use the linear formulation. It does permit the representation of the change in RSS on a specific connection between calibration time t_c and time *t* to be represented as [19]:

$$\Delta y_i = y_i(t) - y_i(t_c) = S_i(t) - S_i(t_c) + F_i(t) - F_i(t_c) + v_i(t) - v_i(t_c) \quad (3)$$

$F_i(t)$ and $v_i(t)$ are two different terms that may be merged to form a single noise term n_i, and Equation (2) can be incorporated to turn Equation (3) into:

$$\Delta y_i = \sum_{j=1}^{N} w_{ij} x_j(t) - \sum_{j=1}^{N} w_{ij} x_j(t_c) + n_i \quad (4)$$

$$\Delta y_i = \sum_{j=1}^{N} w_{ij} \left(x_j(t) - x_i(t_c) \right) + n_i \quad (5)$$

$$\Delta y_i = \sum_{j=1}^{N} w_{ij} \Delta x_i + n_i \quad (6)$$

This may then be expressed vectorially and metrically as:

$$\Delta y = W \Delta x + n \quad (7)$$

Where Δy represents the change in RSS on each link, Δx epresents the change in attenuation in each pixel, *n* represents the measurement noise on each link, and W represents the weight matrix. Contains the weights applied to each connection in pixels [19]. Calibration may be simplified to Equation (8), and the RTI issue can be expressed in a linear form in the interests of discussion.

$$y = Wx + n \quad (8)$$

Many different weight matrices, *W*, connect the RSS to an image.

B. Weight Matrix

The pixel content affects the link's signal intensity, as shown by the weight matrix W. Each connection is represented by a row and each pixel is represented by a column in the matrix. Any weight matrix value in row *l* and column *p* that is nonzero is due to the signal disruption model, which is discussed later in this section and assumes that pixels *p* have an effect on links *L*. Otherwise, the entry is zero [32]. Martin, et al. [33] weight models have been found, and it is hypothesised that each model may be described in terms of a certain weight Equation (9).

$$W = S \odot \Omega \quad (9)$$

Where S is a binary matrix specifying which connections effect which pixels, W is a magnitude matrix defining how links affect pixels in more detail and $\odot$ is the element-wise product of the two matrices. A link m and pixel n may be selected from one of three typical selection matrices in [33] Equation (10) to (12).

$$S_{m,n}^{Ellipse} = \begin{cases} 1, & if\ d_{1,m,n} + d_{2,m,n} < d_m + \lambda \\ 0, & otherwise \end{cases} \quad (10)$$

$$S_{m,n}^{Line} = \begin{cases} 1, & if\ \ link\ m\ intersects\ pixel\ n \\ 0, & otherwise \end{cases} \quad (11)$$

$$S_{m,n}^{All} = 1 \quad (12)$$

Where d_m is the total link length of link m, $d_{1,m,n}$ is the distance from the centre of pixel n to one endpoint of link m, $d_{2,m,n}$ is the distance from the centre of pixel n to the other endpoint of link m, and λ is a parameter that can be selected to determine the length of the major axis of the ellipse that exceeds the length of link m.

Expressed as $\lambda_{m,n} = d_{1,m,n} + d_{2,m,n} - d_m$. The $S^{Ellipse}$ The selection matrix is the most frequently used in literature, found in a variety of RTI publications, including [31], [34]–[36], among many others. An elliptical pattern surrounding the transmitter and receiver conforms to the electromagnetic Fresnel ellipsoid, which is connected to diffraction patterns around an obstacle, as shown in [37], [38].

4. RTI SYSTEM SET UP

Figure 1 shows the suggested setup. Each RF node was encased and evenly spaced. They were configured to receive the scattering field in numerous directions to generate images. This study's experiment arrangement examined a person. The system's hardware is designed based on RF nodes which is ESP8266 wifi operated at frequency of 2.4 GHz. The system has 8 RF nodes, between each node 66.6 cm, monitoring area 200 cm x 200 cm. Essentially, the process tomography technique has several categories depending on the core of the system. In flow measurement, the node array is generally used as the RF node to transmit and receive signals. It is mounted around the area as shown in Figure 1 that needs to measure for data acquisition purposes. The measurement system is dependent upon the core of the system, and the type of desired data to be collected in this system has two methods online. Finally, the image reconstruction algorithms are used to visualise and represent the collected data as an image on the PC.

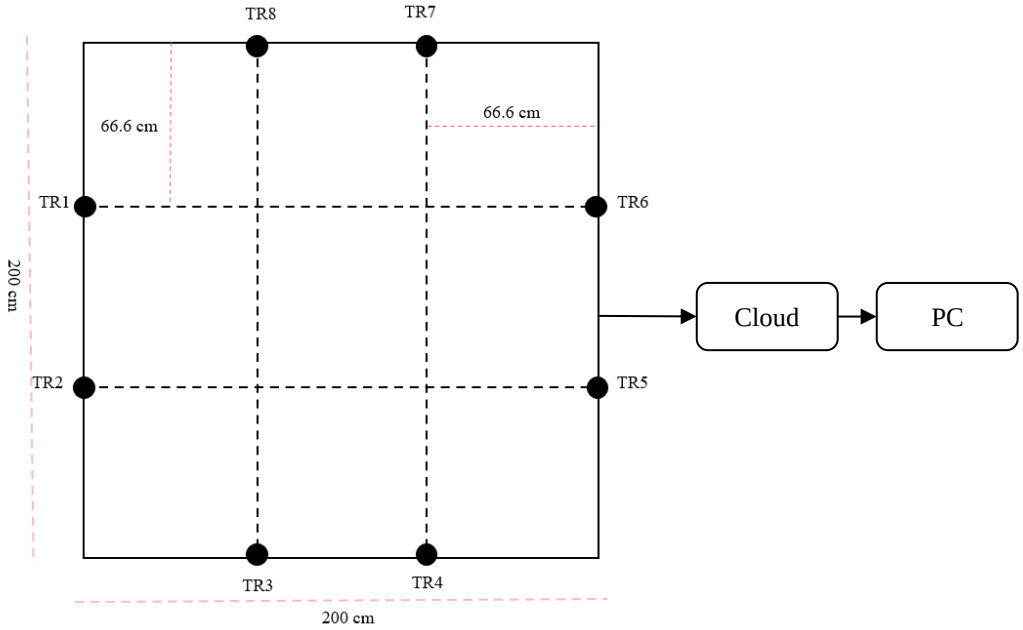

Figure 1 Specification of the system design

The AP's data was sent to the cloud via Message Queue Telemetry Transport MQTT and Firebase. Data is sent to the cloud to monitor RSSI using a computer or a smartphone with internet access. Firebase stores and syncs data across users and devices in real-time, utilising a cloud-hosted NoSQL database. So, data sync across linked devices in milliseconds and stays accessible if applications go offline, as shown in the Figure 2.

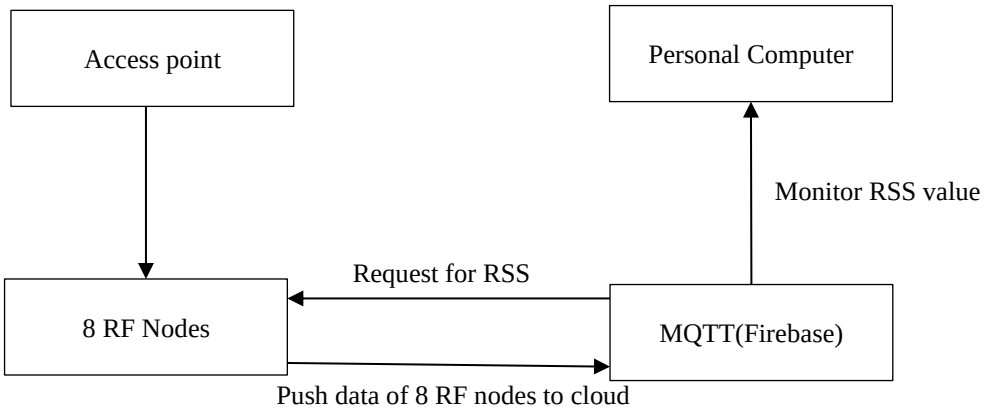

Figure 2. Block diagram of network communication of the system

5. SYSTEM MODELLING

The prototype system proposed in this design has 8 RF nodes transceiver (Rx, Tx) nodes mounted around the monitoring area. The area has a dimension of 200cm x 200cm, and there are 66.6 cm intervals between each node, as shown in Figure 3 a. The model's mathematical computation is a key design aspect that impacts the RF signals and the reconstructed image. RF nodes are placed in a square cavern beside a similar-sized interior area. All projection characteristics, including propagation, frequency, and equations, apply to all RF nodes positioned around the internal square, as shown in Figure 3 b. Frequency propagation determines projection angle. Mixed parallel projection improves image quality[39].

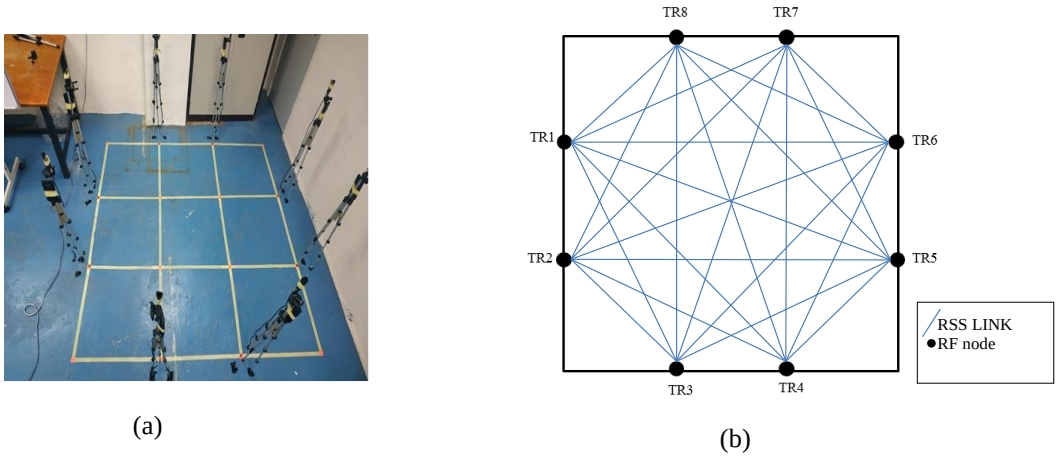

Figure 3. System modelling a) The actual experiment condition b) Model of full projection.

6. SOLVING FORWARD PROBLEM

The forward challenge is to compute each sensor's theoretical output in a two-dimensional segment. Using theoretical sensor outputs, a simulated measuring region will be constructed. The area of interest is mapped onto the arrays as square matrices with dimensions forming 600 × 600 matrices (360,000 pixels). Forward issue solved via sensitivity maps. A sensitivity map projects the effects of a sensor onto a known receiving sensor using weighting matrices that indicate RSS attenuation.

A. Sensitivity maps

The sensitivity function of an array tells us the degree to which a slight change in the resistivity of a section of the sub-surface will influence the potential measured by that array. The higher the sensitivity function's value, the greater the influence of the sub-surface region on the measurement. A different array gives a different type of response over the same sub-surface feature. Some arrays provide better responses over vertical changes, and some deliver better responses for horizontal changes [40]. Different arrays have different sensitivity, depth of investigation and different signal strength [41]. The Jacobian matrix *J*, usually

called the sensitivity map, can be calculated from the electric field strength distribution $\partial E(x,y)$ for different excitations J using the modified perturbation method as shown in Equation (13). One element J_{ji} of this matrix describes the dependency of the measurement data E_{ji} on a change in permittivity of one element $\partial \mathcal{E}_r(x,y)$ of the model [42].

$$J_{ji} = \frac{\partial E(x,y)}{\partial \mathcal{E}_r(x,y)} \tag{13}$$

For the normalized sensitivity maps in the case of air as the reference material, an excitation at port j=1 and measurements at ports i =2,3,4,5,6,7 and 8 are shown in Figure 4 sensitivity maps of excitation at a node j = 1, with the corresponding measurement at nodes i=5 and i=8. Each sensitivity map corresponds to a row vector J_{ij} for a reconstruction mesh, from which the forward model's mesh was generated. It is possible to exclude the dielectric windows from this array. The most sensitive mesh elements are positioned every time between the excitation and measurement ports.

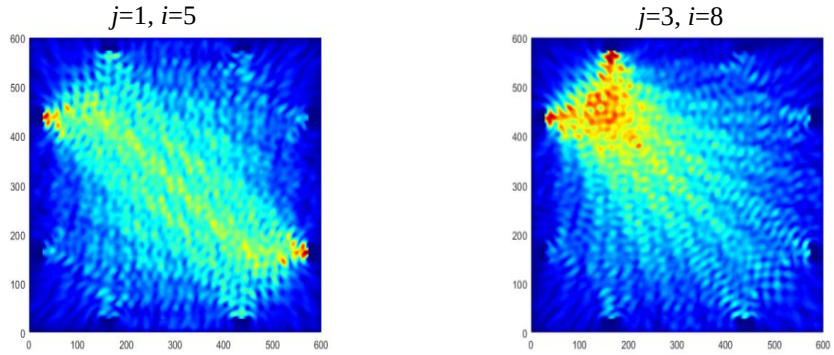

Figure 4. Normalized sensitivity maps of excitation at a node, j = 1, with the corresponding measurement at nodes i=5 and i=8.

7. SOLVING INVERSE PROBLEM

Several qualitative linear and nonlinear For this study, imaging methods were examined. When extracting the dispersed electromagnetic field, this imaging does not offer exact information about the object (person). The electromagnetic field, on the other hand, does reflect certain changes in various objects. To put it another way, qualitative imaging may rebuild a human picture in a WSN for proof of concept in an early investigation. Besides, these qualitative linear imaging approaches are chosen because they are the simplest and fastest to use.

A. Linear Back Projection

Generally, the LBP algorithm is an approach that can reconstruct an image of the unknown density distribution of the human by measuring the RF signals transmitted among transceivers. The LBP algorithm's simplicity and straight forwardness of the LBP algorithm make it a natural choice for image reconstruction in many fields of tomography. Despite its imperfect reconstruction accuracy, LBP has the benefit of being fairly quick, needing simply the multiplication of a fixed reconstruction matrix times the vector of data.

Reconstruction images are applied to extract as much as possible of the internal distribution changes by using a linear back-projection algorithm (LBP). As noted in Equation (14), the LBP algorithm proves its capability, accuracy and contribution in radio system tomography to visualise multiphase components. Although LBP exhibits low-quality reconstruction due to reconstruction artefacts and left/right image roll-offs from the centre of the image, the implementation of LBP is considered a fast and practical function or filter that blurs the image.

$$G_{LBP}\ (\mathrm{x,y}) = \sum_{\mathrm{Tx}=1}^{8} \sum_{\mathrm{Rx}=1}^{7} S_{Tx,Rx} \times M_{Tx,Rx}(\mathrm{x,y}) \tag{14}$$

Where:

$S_{Tx,Rx}$ = $\frac{calibration\ value - measurement\ value}{calibration\ value}$

$M_{Tx,Rx}$ = sensitivity maps

B. filtered back projection

Filtered back-projection is one of the analytical approaches for image reconstruction algorithms used in various fields of tomography, and it has the capability of removing noise (left/right blurring occurs in

linear back projection) using a filter, which is a matrix with the exact dimensions as the Jacobian matrix in the LBP algorithm, as shown in Equation (15), which can be expressed mathematically[43]. The filter is constructed by identifying the highest pixel in the sensitivity matrix.

$$G_{\mathrm{FBP}}(\mathrm{x,y}) = \mathrm{F(x,y)} \times G_{\mathrm{LBP}}(\mathrm{x,y}) \tag{15}$$

Equation (16) shows the maximum pixel value in the weight-balanced map, and P_{max} is divided by the weight-balanced map, W_n, to obtain the filter matrix $F(x,y)$.

$$F = \frac{P_{max}}{W_n} \tag{16}$$

Where $G_{\mathrm{FBP}}(\mathrm{x,y})$ is the filter back − projection, $F(x,y)$ is filter matrix, P_{max} is a maximum pixel value in a weight-balanced map and W_n is the weight balanced map.

C. Gaussian Algorithm

The model is based on the log-distance path loss model, one of many radio signal propagation models. The log-distance path loss model is defined in Equation (17) [44].

$$PL_d = PL_{d0} + 10\gamma\, log_{10}\left(\frac{d}{d_0}\right) + \chi \tag{17}$$

Where PL_d is the path loss at distance d in decibels, d_0 is a reference distance (usually 1 m) for which the signal strength is measured, γ is the path loss exponent (determined empirically for different environments), and χ is a Gaussian random variable. The log-distance path loss model, therefore, models environmental noise using a Gaussian random variable. This observation, together with the idea that a pixel should have less weight when it is farther away from the line of sight (LOS) path, led to the idea of using a Gaussian distribution for the weight assignment. The general Gaussian function is defined in Equation (18).

$$f(x) = \alpha e^{-\frac{(x-\mu)^2}{2\sigma^2}} \tag{18}$$

Where α is the height of the curve's peak, μ is the location of the peak's centre, and σ is the standard deviation that controls the width of the top of the curve. The Gaussian model uses the Gaussian function to assign weights for the pixels. The idea is to give the most weight to pixels on the LOS path and less weight farther away, depending on their distance from the LOS path.

D. Newton's One-Step Error Reconstruction

Newton's one-step error reconstruction (NOSER) is a fast and practical algorithm for producing qualitative images [45]. Equations (19) to (21) show the NOSER formula for the RTI system.

$$G_{NOSER}(x,y) = \sum_{j=1}^{T}\sum_{i=1}^{R}[H]^{-1} \times LS_{ji} \times J_{ji}(x,y) \tag{19}$$

$$LS_{ji} = \left[S_{ij}^{tot} - S_{ij}^{inc}\right]^2 \tag{20}$$

$$H = J_{ji}(x,y) * \left[J_{ji}(x,y)\right]^T \tag{21}$$

Where LS_{ji} is sensor loss calculated in the least square method, and H is the Hessian matrix. The least square method aims to minimize the variation between the S_{ij}^{inc} and S_{ij}^{tot} for a given electric field distribution in computational domain [42]. Besides, Hessian matrix is not square when the electrodes and air are excluded in the reconstruction. It is impossible to compute the direct inverse. Transposed matrix is utilized as a rough approximation instead of inverse [45], [46]. Hence, the NOSER formula is rewritten as in Equation (22) for the RTI system.

$$G_{NOSER}(x,y) = [H]^T \times \sum_{j=1}^{T}\sum_{i=1}^{R} LS_{ji} \times J_{ji}(x,y) \tag{22}$$

E. Tikhonov Regularization

Tikhonov Regularization (TR) is the most widely used method in linear inverse problems and for regularising the update problem in linear RTI [47]. From literature, these are a few examples that can be referred to [48]–[50]. It chooses a single solution from the infinite number of possible solutions and stabilizes the solution technique so that the noise in the data does not direct to considerable modifications in the final result [51]. Initially, the process of minimization of S_{ij}^{inc} and S_{ij}^{tot} has to be done. Next, the singular value decomposition is utilized to analyse the solution. In this study, summation of Hessian matrix is decomposed into three constituent matrices which are U, $\sum$ and V. U and V are unitary matrices and $\sum$ is a diagonal matrix. The diagonal elements of $\sum$ are the singular values, ρ in Equation (23) decays gradually to zero when

the matrix is ill-conditioned. The solution is represented by Equation (24) which its denominator will never equivalent to zero as *ρ> 0 and* it reduces noises in the measured data onto the absolute solution [51].

$$\rho = diag(\sum) \tag{23}$$

$$T_{tikh,k} = \frac{\rho}{\rho^2 + k} \tag{24}$$

where k is the regularization parameter and $k > 0$. The formula to reconstruct the image with the implementation of TR is expressed in Equation (25) for the RTI system.

$$G_{tikh,\alpha} = U \times V \times diag(T_{tikh,k}) \times \sum_{j=1}^{T} \sum_{i=1}^{R} LS_{ji} \times J_{ji} \tag{25}$$

Tikhonov's smoothing approach is determined by the regularization parameter. The different regularization parameter, k value is applied for 8 RTI system to achieve final reconstructed image.

8. NORMAL DISTRIBUTION

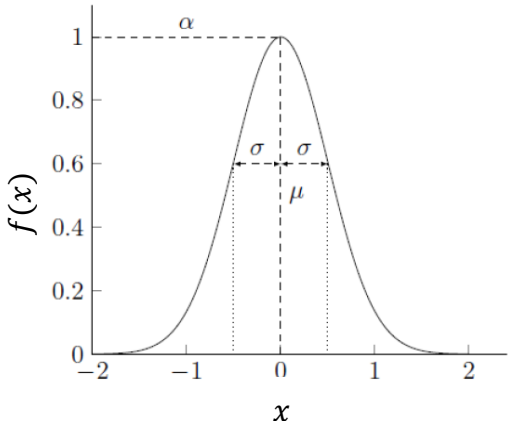

Figure 5. Probability density function of a normal distribution N (μ, σ), with mean μ and standard deviation σ > 0.

Consider a sample $x_1, x_2, \ldots, x_n$ drawn from a normal distribution. Each data measurement, x_i is given accuracy of $\pm\varepsilon/2$. Assuming that ε is small, the probability density function of *N(μ,σ)* can be approximated as a constant over $\left[x_i - \frac{\varepsilon}{2}, x_i + \frac{\varepsilon}{2}\right]$ as explained in [52]. The length for the sample is therefore:

$$\sum_{i=1}^{n}\{-In(\varepsilon\, f(x_i))\} = \sum_{i=1}^{n}\left\{-In\left(\frac{\varepsilon}{\sqrt{2\pi\sigma}}\right) + \frac{1}{2}\left|\frac{x_i-\mu}{\sigma}\right|^2\right\} \tag{26}$$

By setting μ equal to the sample mean (m), and μ can only be stated to a finite accuracy, $\pm b/2$. Leaving σ fixed, μ having the value m, state it within $\left[m - \frac{b}{2}, m + \frac{b}{2}\right]$, assumed that μ as *a priori* to lie in range of size a, therefore takes $\ln\left(\frac{b}{a}\right)$, to state μ to accuracy $\pm\frac{b}{2}$ to $\ln\left(\frac{b}{a}\right)$. similarly to μ, σ is known *a prior* to lie in $[0 \ldots p]$. Is stated to have an accuracy $\pm c/2$. So $\ln\left(\frac{c}{p}\right)$ to state σ to within $\pm\frac{c}{2}$: $\ln\left(\frac{c}{p}\right)$.

Note that sample standard, z is given by Equation (27).

$$z = \sqrt{\sum_{i=1}^{n} \frac{(x_i - m)^2}{n}} \tag{27}$$

This is a biased estimator for σ; consider *n=1, or n=2,* although there is little bias for large values of *n*. replacing the divisor, *n*, $(n-1)$. The accuracy with which $\mu(\pm\frac{b}{2})$ and $\sigma\left(\pm\frac{c}{2}\right)$ should be state is found by adding contribution from the data, μ, *and* σ, choosing *b* and *c* to minimise the expected total:

$$-\ln\left(\frac{b}{a}\right) - \ln\left(\frac{c}{p}\right) + \sum_{i=1}^{n}\left\{-\ln\left(\frac{\varepsilon}{\sqrt{2\pi\sigma}}\right) + \frac{1}{2}\left|\frac{x_i-\mu}{\sigma}\right|^2\right\}$$

$$= -\ln\left(\frac{bc}{ap}\right) - n\,\ln\left(\frac{\varepsilon}{\sqrt{2\pi\sigma}}\right) + \sum_{i=1}^{n}\left\{\frac{1}{2}\left|\frac{x_i-\mu}{\sigma}\right|^2\right\} \tag{28}$$

And noting that $\left(x_i - m - (\mu - m)\right)^2 = (x_i - m)^2 - (2x_i - m)(\mu - m) + (\mu - m)^2$ and that $\sum_{i=1}^{n}(x_i - m) = 0$

$$-\ln\left(\frac{bc}{ap}\right) - n\ \ln\left(\frac{\varepsilon}{\sqrt{2\pi\sigma}}\right) + n\frac{\{z^2+(\mu-m)^2\}}{2\sigma^2} \tag{29}$$

The expectation of $(\mu - m)^2$ over $\left[m - \frac{b}{2}, m + \frac{b}{2}\right]$, and assuming a uniform distribution in this rang, is $\left(\frac{1}{b}\right)\left[\frac{b^3}{3}\right]_{\frac{-b}{2}\cdots\frac{b}{2}} = \frac{\left(\frac{2b^3}{24}\right)}{b} = \frac{b^2}{12}$. The differentiate with respect to *b* and:

$$-\frac{1}{b} + n\frac{b}{12\sigma^2} = 0 \tag{30}$$

$$b = \sigma\sqrt{\frac{12}{n}} \tag{31}$$

Substituting this value for *b*:

$$\begin{aligned} &-\ln\left(\frac{c}{p}\right) - \ln\left(\frac{\sigma}{a}\sqrt{\frac{12}{n}}\right) - n\ln\left(\frac{\sigma}{\sqrt{2\pi\sigma}}\right) + n\frac{(z^2+\frac{\sigma^2}{n})}{2\sigma^2} \\ &= -\ln\left(\frac{c}{p}\right) - \ln\left(\frac{\sigma}{a}\sqrt{\frac{12}{n}}\right) - n\ln\left(\frac{\sigma}{\sqrt{2\pi\sigma}}\right) + \frac{n\,z^2}{2\sigma^2} + \frac{1}{2} \end{aligned} \tag{32}$$

To find the optimal value of σ, which interestingly turn out to differ from *z*, differentiate with respect to $\sigma$and set to 0:

$$\frac{n-1}{\sigma} = \frac{n\,z^2}{\sigma^3} \tag{33}$$

$$\sigma = z\sqrt{\frac{n}{(n-1)}} \tag{34}$$

Now σ can only be stated to finite accuracy, being in the range $\left[\frac{\acute{\sigma}-c}{2}, \frac{\acute{\sigma}+c}{2}\right]$. similarly to $\mu - m$, the expectation of $(\sigma - \acute{\sigma})^2$ is $\frac{c^2}{12}$.

Let $\sigma = \acute{\sigma}\ (1 + h)$ in Equation (32).

$$\begin{aligned} &-\ln\left(\frac{c}{p}\right) - \ln\left(\frac{\sigma}{a}\sqrt{\frac{12}{n}}\right) - n\ln\left(\frac{\sigma}{\sqrt{2\pi\sigma}}\right) + \frac{n\,z^2}{2\sigma^2} + \frac{1}{2} \\ &= -\ln(c) + (n-1)\ \ln(1+h) + \frac{n\,z^2}{2(\sigma^2)(1+h)^2} + \{terms\ independent\ of\ h\} \\ &= -\ln(c) + (n-1)\left(\frac{h-h^2}{2}\right) + n\,z^2\frac{\left(1-2h+3h^2\right)}{2\sigma^2} + (0h^3) + \{terms\ no\ h\} \end{aligned} \tag{35}$$

Assuming that the fractional error *h* in stating the standard deviation is small:

$$\begin{aligned} &-\ln(c) + h\left((n-1) - \frac{nz^2}{\sigma^2}\right) + h^2\left(\frac{-(n-1)}{2} + \frac{3nz^2}{2\sigma^2}\right) + n\frac{z^2}{2\sigma^2} \\ &= -\ln(c) + h^2(n-1) \end{aligned} \tag{36}$$

Where $(n-1)\sigma^2 = nz^2$. So $h = \frac{(\sigma-\acute{\sigma})}{\acute{\sigma}}$ and the expectation $E(h^2) = \frac{c^2}{12\,\acute{\sigma}^2}$ putting in Equation (36).

$$-\ln(c) + \frac{c^2(n-1)}{12\,\sigma^2} \tag{37}$$

Differentiate with respect to *c* and to 0:

$$\frac{1}{c} = c^2\frac{(n-1)}{12\,\sigma^2} \tag{38}$$

$$c = \sigma\sqrt{\frac{6}{(n-1)}} \tag{39}$$

9. RESULTS AND DISCUSSION

A. *Calibration*

The calibration of the RTI system was done in two stages. The first measured the RSS value when the experiment area was empty, and the second measured using obstacle (human). Figure 6 shows the RSS value of both measurement calibration and measurement. The RSS values in the calibration of the system for all 8 RF nodes of the system were in the range of $-23\text{dBm} \leq x \leq -25\text{dBm}$ when the zone was empty, and the RSS values of humans were in the range $-42\text{dBm} \leq x \leq -52\text{dBm}$.

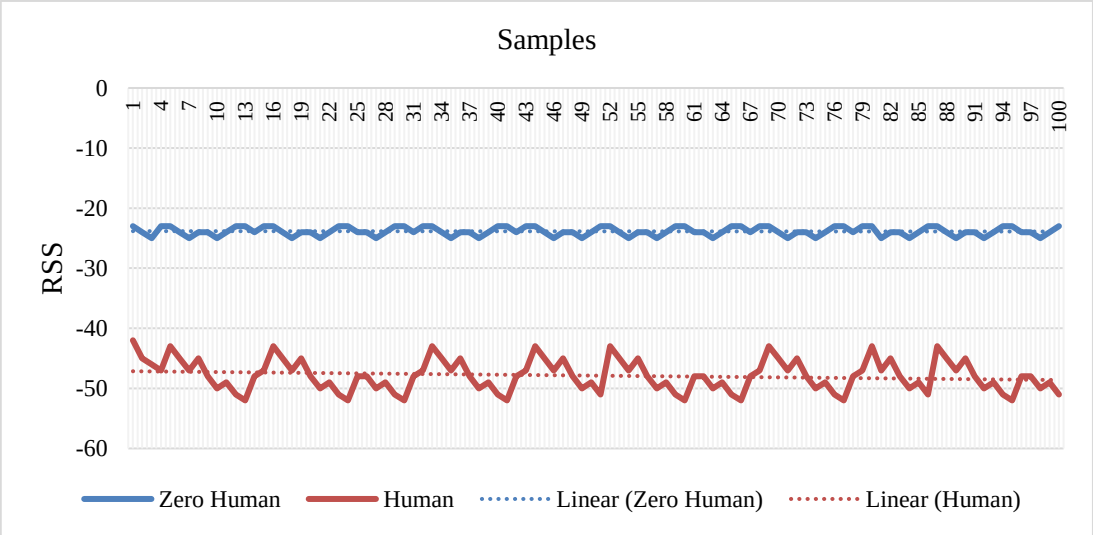

Figure 6. The RSSI signals measured by the target node (TR1= 2 m, TR3= 2 m); with humans.

The system can identify the presence of intruders, and it triggers a feedback loop that has a substantially more significant standard deviation and variance in an inhabited room with an obstacle which was human [53]. Even from Table 2, we can deduce that statistics like variance and standard deviation are great for detecting intrusions.

Table 2. Data statistic of RSSI for 100 cycles between two nodes.

Condition	Zero Human	1 Person
Min[dB]	-25	-52
Max[dB]	-23	-42
Mean(μ)[dB]	-23.86	-47.88
Std dev. (σ)	0.73	2.62
Var (σ^2)	0.53	6.85

Furthermore, one of the characteristics to emphasise in this part is the change in variance. The variance was computed so that the system could determine the difference in RSS readings from the average. The variance for the empty zone was approximate $-23\text{dBm} \leq x \leq -26\text{dBm}$; however, when the human was detected inside the area, the difference in RSS value increased between -15 dBm to -25 dBm.

B. Experimental Results

The radio tomography system's core is its reconstruction algorithms, which aid in seeing the interior distribution. The RTI reconstruction used MATLAB regularisation. The image reconstruction algorithms applied in the system were The LBP, FBP, Gaussian, NOSER and TR algorithms, and the image quality of the reconstructed images was evaluated with the MSSIM image quality assessment to conclude the outcomes of the proposed radio tomography system. Three tests were carried out to test and assess the suggested technique for the various algorithms. Each algorithm has its own set of characteristics and mathematical qualities. In this research, the various proposed phantoms EXP.1, EXP.2 and EXP.3 have been tested to reconstruct the tomography imaging, as shown in Table 3. The Colour scale is used to represent the human concentration in the tomogram, the blue colour was air, and the red colour was a human stand in the monitoring area. It can be observed that the higher intensity spot (red colour) is more concentrated in the targeted location, which represents the human phantoms. However, these reconstructed images also illustrated that, as the number and size of the human phantoms increased, the smearing artefacts increasingly marked up the imaging results, which eventually amplified the image noise floor. This condition is primarily reflected by the LBP and FBP algorithms compared to the NOSER and Tikhonov Regularisation algorithms. The LBP and FBP algorithms are well understood for their poor accuracy due to the appearance of artefacts conceivably caused by the back- projection techniques.

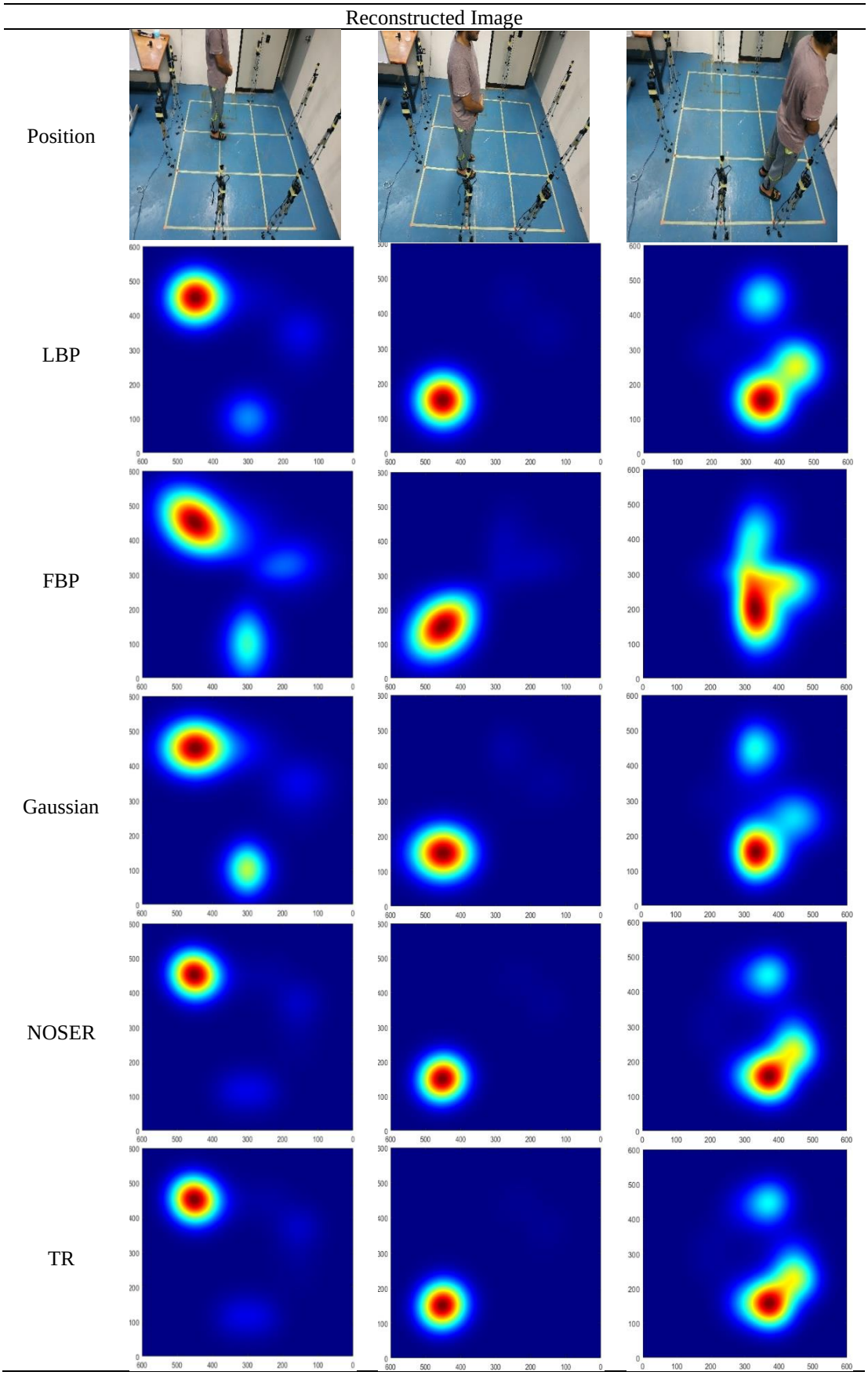
Reconstructed Image
Position
LBP
FBP
Gaussian
NOSER
TR

In contrast, the NOSER and Tikhonov Regularisation algorithms have visually improved the reconstructed tomogram images for all rice phantoms' profiles. The improvement in minimising the smearing artefacts by these algorithms is believed to be yielded through solving the inverse problem using the non-linear approach. The image reconstruction results across all algorithms are then quantified using MSSIM indexes. The MSSIM quantification is carried out due to its excellent performance. The tomography system could identify all the test profiles based on the static experiment findings. In the modelling part, a single individual was identified as being detectable. A human High Low-test profile was used to test this restriction, and the findings demonstrate that all five reconstruction algorithms could identify the human profile. This is obvious proof that the modelling in this study was proved. The maximum detection of humans will be tested later for multiple targets.

C. Sigma analysis

Statistics and sigma use the normal distribution as a shared continuous probability distribution. An informal term for it is "overall Mathematical Model," which describes the distribution of the data set. The first inflection point of the normal distribution occurs at one standard deviation from its mean, and the area under the curve and over the x-axis is equal to one. As a result, about 68% of values taken from a normal distribution lie within one standard deviation (σ) of the mean, approximately 95% of values fall within two standard deviations, and approximately 99.7% of values lay within three standard deviations. An important idea in statistical process control is that 99.7% of the data in a collection with a normally distributed distribution are within three standard deviations of the mean.

Therefore, from the comparison of the different sigma, 0.8 sigma was the best overall also from the comparison of the different algorithms, based on Table 4 and Figure 7 to 9, for experiments EXP.1, EXP.2, and EXP.3, When sigma equals 0.8, the NOSER and TR algorithms performed best for the MSSIM index. Meanwhile, the Gaussian MSSIM index increased just somewhat when compared to the NOSER and TR MSSIM indexes. As a result, it seems that the NOSER and TR algorithms are the best techniques for producing pictures that look similar to the original images, followed by Gaussian, LBP, and FBP since they have the greatest scores across all reconstructed images. Finally, the NOSER and TR algorithms have the greatest overall value across all experiments, indicating that they are better than the other methods.

Table 4. Different value of sigma with MSSIM indexes computed on reconstructed images.

SIGMA	EXP.1					EXP.2					EXP.3				
	LBP	FBP	GAUSSIAN	NOSER	TR	LBP	FBP	GAUSS	NOSER	TR	LBP	FBP	GAUSN	NOSE	TR
0.1	0.2204	0.2204	0.2205	0.2212	0.2212	0.2202	0.2201	0.2201	0.2205	0.2205	0.2236	0.2242	0.2219	0.2222	0.2222
0.2	0.2254	0.2254	0.2267	0.2246	0.2246	0.2234	0.2224	0.222	0.2237	0.2237	0.2367	0.2412	0.2321	0.2315	0.2315
0.3	0.2351	0.2473	0.2432	0.2308	0.2308	0.2332	0.2346	0.231	0.2334	0.2334	0.2598	0.2616	0.2573	0.2487	0.2487
0.4	0.2676	0.2837	0.2689	0.2439	0.2439	0.2528	0.2629	0.2544	0.249	0.279	0.2867	0.2842	0.2917	0.2785	0.2785
0.5	0.3098	0.3465	0.3101	0.2869	0.2869	0.2771	0.3024	0.2854	0.2672	0.2872	0.3235	0.3139	0.3275	0.3206	0.3206
0.6	0.4007	0.4217	0.3999	0.3586	0.3686	0.3242	0.3806	0.3414	0.2997	0.3197	0.3819	0.3486	0.3798	0.3758	0.3758
0.7	0.4678	0.4053	0.4487	0.4634	0.4734	0.4367	0.4452	0.4561	0.3844	0.3894	0.4006	0.3771	0.4015	0.4172	0.4172
0.8	0.4485	0.3759	0.4142	0.4856	0.4956	0.5178	0.4532	0.4838	0.4959	0.5089	0.3933	0.3941	0.4201	0.4575	0.4675
0.9	0.3918	0.3390	0.3621	0.4438	0.4538	0.4860	0.4362	0.4323	0.4716	0.4926	0.3880	0.4069	0.398	0.3998	0.3998

Table 5. Data statistic of RSSI for 100 cycles for one person at three locations.

Condition	EXP.1					EXP.2					EXP.3				
	LBP	FBP	GAUSSIAN	NOSER	TR	LBP	FBP	GAUSSIAN	NOSER	TR	LBP	FBP	GAUSSIAN	NOSER	TR
Min	0.2204	0.2204	0.2205	0.2212	0.2212	0.2202	0.2201	0.2201	0.2205	0.2205	0.2236	0.2242	0.2219	0.2222	0.2222
Max	0.4678	0.4217	0.4487	0.4856	0.4956	0.5178	0.4532	0.4838	0.4959	0.5089	0.4006	0.4069	0.4201	0.4575	0.4675
Mean(μ)	0.3297	0.3184	0.3216	0.3288	0.3332	0.3302	0.3286	0.3252	0.3262	0.3283	0.3216	0.3169	0.3255	0.3280	0.3291
Std dev.(σ)	0.0988	0.0769	0.0872	0.1106	0.1155	0.1186	0.1002	0.1068	0.1077	0.1113	0.0718	0.0681	0.0776	0.0877	0.0895
Var (σ^2)	0.0098	0.0059	0.0076	0.0122	0.0133	0.0141	0.0100	0.0114	0.0116	0.0124	0.0052	0.0046	0.0060	0.0077	0.0080

The system can identify the presence of intruders. It generates a feedback loop that has a substantially more significant standard deviation and variance in an inhabited room than it does in an empty room. Even from Table 5, the system can deduce that statistics like variance and standard deviation are great for detecting intrusions.

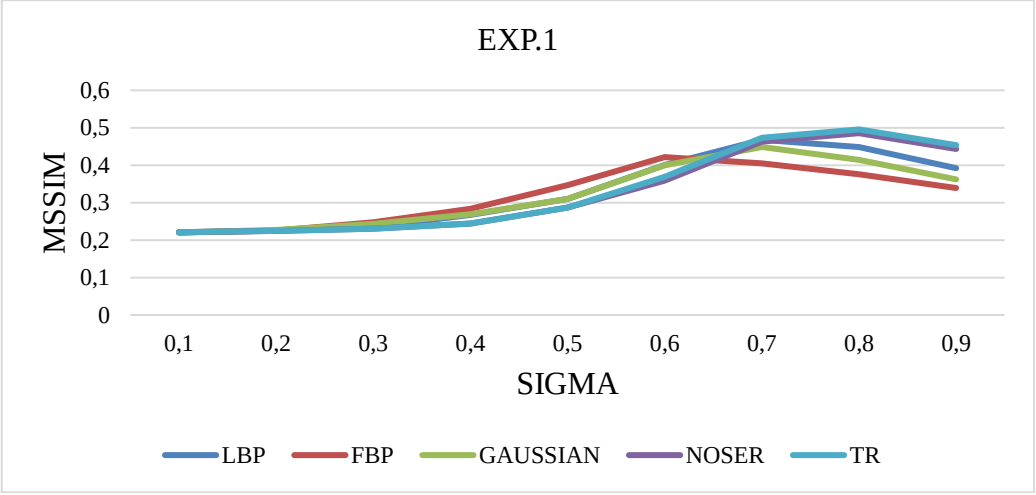

Figure 7. MSSIM indexes calculated on reconstructed images based on sigma (EXP.1).

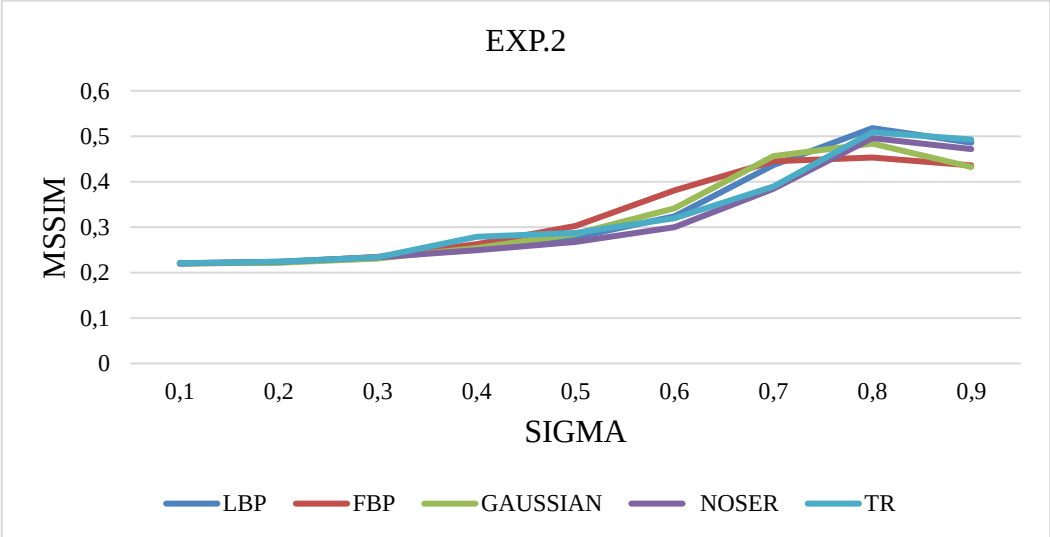

Figure 8. MSSIM indexes calculated on reconstructed images based on sigma (EXP.2).

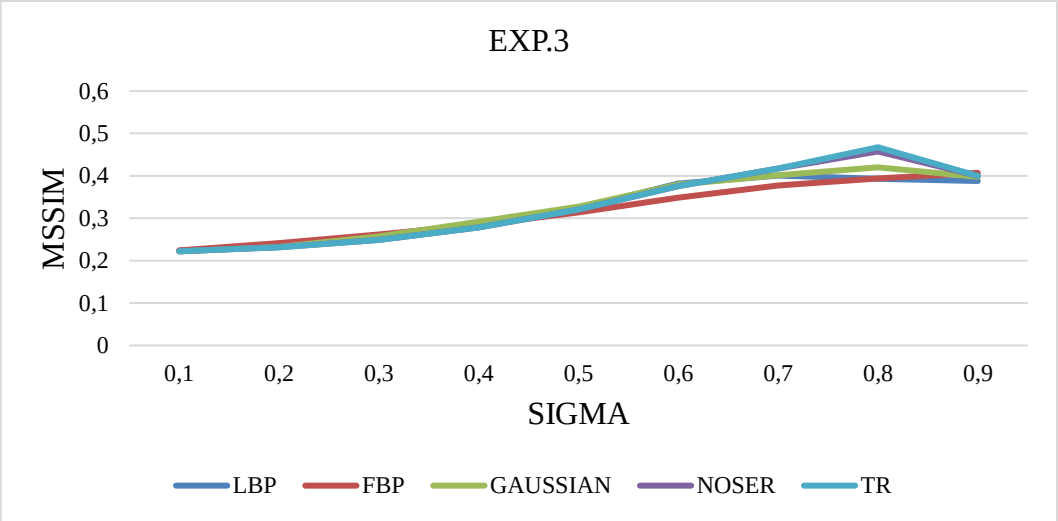

Figure 9. MSSIM indexes calculated on reconstructed images based on sigma (EXP.3).

D. Mean Structural Similarity Analysis

Image quality was evaluated using the Mean Structural Similarity Index (MSSIM) evaluation tool. Figure 10 shows the EXP.1, EXP.2 and EXP.3 in different locations. In this experiment, five reconstruction algorithms were involved. As shown in Table 6, all the phantoms were in a background of air, which was used as the reference. A comparison among the frequencies is made for the different algorithms, and it is found that the NOSER and TR algorithm has the highest value overall (0.4959) (0.508895), respectively. For the Gaussian algorithm in the tests for the three experiments, the highest value was 0.50376; for the FBP algorithm, the highest value was 0.453221; and for the LBP algorithm, the highest value was 0.

Table 6. MSSIM indexes computed on reconstructed images of the experiment

Algorithm	Experiment		
	EXP.1	EXP.2	EXP.3
LBP	0.448516	0.447774	0.393272
FBP	0.37589	0.453221	0.39406
GAUSSIAN	0.414206	0.50376	0.399988
NOSER	0.495585	0.508895	0.407536
TIKHONOV	0.495585	0.508895	0.407536

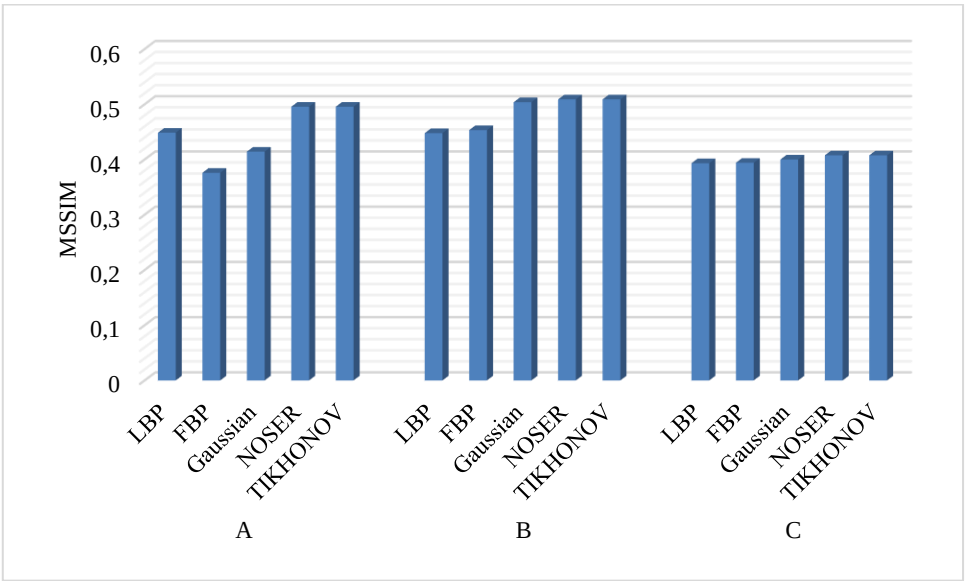

Figure10. MSSIM indexes calculated on reconstructed images of experiment

However, the MSSIM result suggests a low index for all phantoms. The maximum score was acquired for experiment B with an index value of 0.508895 using the NOSER and TR algorithms, while the lowest score was obtained for experiment A with an index value of 0.37589 using the FBP method. In general, the NOSER, TR, and Gaussian approaches performed well and resulted in an increase in the MSSIM index.

10. CONCLUSION

Radio tomography imaging for human localization has been successfully developed, the evaluation and analysis of its performances was made by using minimum number of RF nodes. The sigma was proposed to solve the issue with low spatial resolution image by reducing the noise. Several experiments were conducted, and the results had showed encouraging improvement in tomogram reconstruction using sigma method where a 0.8 of sigma was the best of overall. NOSER and TR algorithms scored the highest for the MSSIM index overall experiments, and it is the best technique to produce images that appear similar to the original images.

ACKNOWLEDGEMENTS

The authors would like to acknowledge the sup- port from the Transdisciplinary Research Grant Scheme (TRGS) under grant number of TRGS/1/2018/UNIMAP/02/4/2 from the Ministry of Higher Education Malaysia. The authors would also gratefully thank Universiti Malaysia Perlis, Malaysia for the facilities and technical assistance.

REFERENCES

[1] S. Shukri and L. M. Kamarudin, "Device free localization technology for human detection and counting with RF sensor networks: A review," *J. Netw. Comput. Appl.*, vol. 97, no. October 2016, pp. 157–174, 2017, doi: 10.1016/j.jnca.2017.08.014.

[2] J. Zhang, W. Xiao, and Y. Li, "Data and Knowledge Twin Driven Integration for Large-Scale Device-Free Localization," *IEEE Internet Things J.*, vol. 8, no. 1, pp. 320–331, 2021, doi: 10.1109/JIOT.2020.3005939.

[3] L. Zhao, C. Su, H. Huang, Z. Han, S. Ding, and X. Li, "Intrusion detection based on device-free localization in the era of IoT," *Symmetry (Basel).*, vol. 11, no. 5, pp. 1–15, 2019, doi: 10.3390/sym11050630.

[4] Y. Sun, X. Zhang, X. Wang, and X. Zhang, "Device-Free Wireless Localization Using Artificial Neural Networks in Wireless Sensor Networks," *Wirel. Commun. Mob. Comput.*, vol. 2018, 2018, doi: 10.1155/2018/4201367.

[5] O. Kaltiokallio, H. Yigitler, and R. Jantti, "A three-state received signal strength model for device-free localization," *IEEE Trans. Veh. Technol.*, vol. 66, no. 10, pp. 9226–9240, 2017, doi: 10.1109/TVT.2017.2701399.

[6] Y. Sasiwat, N. Jindapetch, D. Buranapanichkit, and A. Booranawong, "An Experimental Study of Human Movement Effects on RSSI Levels in an Indoor Wireless Network," *BMEiCON 2019 - 12th Biomed. Eng. Int. Conf.*, pp. 6–10, 2019, doi: 10.1109/BMEiCON47515.2019.8990208.

[7] Y. Wu, F. Tang, and H. Li, "Image-based camera localization : an overview," pp. 1–13, 2018.

[8] Z. Zhang and X. Gao, "Moving Targets Detection and Localization in Passive Infrared Sensor Networks," *IEEE*, 2007, doi: 10.1109/ICIF.2007.4408178.

[9] R. Priyadarshini and R. M. Mehra, "Quantitative Review of Occupancy Detection Technologies," no. January, 2015.

[10] C. Y. Chiu and D. Dujovne, "Experimental characterization of radio tomographic imaging using Tikhonov's regularization," *2014 IEEE Bienn. Congr. Argentina, ARGENCON 2014*, pp. 468–472, 2014, doi: 10.1109/ARGENCON.2014.6868537.

[11] S. Xu, H. Liu, F. Gao, and Z. Wang, "Compressive sensing based radio tomographic imaging with spatial diversity," *Sensors (Switzerland)*, vol. 19, no. 3, 2019, doi: 10.3390/s19030439.

[12] D. Piumwardane *et al.*, "Poster abstract: An empirical study of WiFi-based radio tomographic imaging," *SenSys 2017 - Proc. 15th ACM Conf. Embed. Networked Sens. Syst.*, vol. 2017-Janua, pp. 5–6, 2017, doi: 10.1145/3131672.3136983.

[13] V. Smallbon, T. Potie, M. D'Souza, A. Postula, and M. Ros, "Implementation of radio tomographic imaging based localisation using a 6LoWPAN wireless sensor network," *WINSYS 2015 - 12th Int. Conf. Wirel. Inf. Networks Syst. Proceedings; Part 12th Int. Jt. Conf. E-bus. Telecommun. ICETE 2015*, pp. 27–32, 2015, doi: 10.5220/0005513400270032.

[14] Z. Wang, H. Liu, X. Ma, J. An, and S. Xu, "Enhancing indoor radio tomographic imaging based on interference link elimination," *Digit. Signal Process. A Rev. J.*, vol. 44, no. 1, pp. 26–36, 2015, doi: 10.1016/j.dsp.2015.05.008.

[15] J. Lu, W. Ke, J. Jin, and Y. Wang, "Radio Tomographic Imaging Based On Quartile Outliers Filter and PCA," *DEStech Trans. Comput. Sci. Eng.*, no. wicom, pp. 285–292, 2018, doi: 10.12783/dtcse/wicom2018/26276.

[16] J. Tan, Q. Zhao, X. Guo, X. Zhao, and G. Wang, "Radio Tomographic Imaging Based on Low-Rank and Sparse Decomposition," *IEEE Access*, vol. 7, no. April, pp. 50223–50231, 2019, doi: 10.1109/ACCESS.2019.2910607.

[17] Q. Wang, H. Yiğitler, R. Jäntti, and X. Huang, "Localizing Multiple Objects Using Radio Tomographic Imaging

Technology," *IEEE Trans. Veh. Technol.*, vol. 65, no. 5, pp. 3641–3656, 2016, doi: 10.1109/TVT.2015.2432038.
[18] A. Mishra, U. K. Sahoo, and S. Maiti, "Sparsity-enabled radio tomographic imaging using quantized received signal strength observations," *Digit. Signal Process. A Rev. J.*, vol. 127, p. 103576, 2022, doi: 10.1016/j.dsp.2022.103576.
[19] J. Wilson and N. Patwari, "Radio tomographic imaging with wireless networks," *IEEE Trans. Mob. Comput.*, vol. 9, no. 5, pp. 621–632, 2010, doi: 10.1109/TMC.2009.174.
[20] M. Bocca, O. Kaltiokallio, and N. Patwari, "Radio tomographic imaging for ambient assisted living," *Commun. Comput. Inf. Sci.*, vol. 362 CCIS, pp. 108–130, 2013, doi: 10.1007/978-3-642-37419-7_9.
[21] Y. Zhao, N. Patwari, J. M. Phillips, and S. Venkatasubramanian, "Radio tomographic imaging and tracking of stationary and moving people via kernel distance," *IPSN 2013 - Proc. 12th Int. Conf. Inf. Process. Sens. Networks, Part CPSWeek 2013*, pp. 229–240, 2013, doi: 10.1145/2461381.2461410.
[22] J. Wilson and N. Patwari, "A Fade-level skew-laplace signal strength model for device-free localization with wireless networks," *IEEE Trans. Mob. Comput.*, vol. 11, no. 6, pp. 947–958, 2012, doi: 10.1109/TMC.2011.102.
[23] F. Thouin, S. Nannuru, and M. Coates, "Multi-target tracking for measurement models with additive contributions," *Fusion 2011 - 14th Int. Conf. Inf. Fusion*, 2011.
[24] M. Bocca, O. Kaltiokallio, N. Patwari, and S. Venkatasubramanian, "Multiple target tracking with rf sensor networks," *IEEE Trans. Mob. Comput.*, vol. 13, no. 8, pp. 1787–1800, 2014, doi: 10.1109/TMC.2013.92.
[25] I. Sabek, M. Youssef, and A. V. Vasilakos, "ACE: An accurate and efficient multi-entity device-free WLAN localization system," *IEEE Trans. Mob. Comput.*, vol. 14, no. 2, pp. 261–273, 2015, doi: 10.1109/TMC.2014.2320265.
[26] M. Maj, T. Rymarczyk, K. Kania, K. Niderla, M. Styla, and P. Adamkiewicz, "Application of the Fresnel zone and Free-space Path for image reconstruction in radio tomography," *2019 Int. Interdiscip. PhD Work. IIPhDW 2019*, pp. 30–33, 2019, doi: 10.1109/IIPHDW.2019.8755429.
[27] M. S. M. Abdullah, L. M. Kamarudin, M. H. F. Rahiman, M. H. F. Rahiman, L. Mohamed, and A. Zakaria, "Simulation of Radio Tomographic Imaging for Measurement Rice Moisture Content," in *2020 10th IEEE International Conference on Control System, Computing and Engineering (ICCSCE)*, 2020, pp. 62–67. doi: 10.1109/ICCSCE50387.2020.9204958.
[28] D. Hutchison and J. C. Mitchell, *Pervasive computing*. 2010.
[29] H. Yigitler, R. Jantti, O. Kaltiokallio, and N. Patwari, "Detector Based Radio Tomographic Imaging," *IEEE Trans. Mob. Comput.*, vol. 17, no. 1, pp. 58–71, 2017, doi: 10.1109/tmc.2017.2699634.
[30] G. Nafziger, "Wireless Sensor Network Optimization for Radio Tomographic Imaging," no. March, 2020.
[31] J. Wilson and N. Patwari, "See-Through Walls : Motion Tracking Using Variance-Based Radio Tomography Networks," vol. 10, no. 5, pp. 612–621, 2011.
[32] T. Van Der Meij, "Computer Science Mobile radio tomography : Reconstructing and visualizing objects in wireless Name : Date :," Leiden University, 2016.
[33] R. K. Martin, A. Folkerts, and T. Heinl, "Accuracy vs . Resolution in Radio Tomography," *IEEE Trans. SIGNAL Process.*, vol. 62, no. 10, pp. 2480–2491, 2014.
[34] A. T. Mobashsher, A. Mahmoud, and A. M. Abbosh, "Portable Wideband Microwave Imaging System for Intracranial Hemorrhage Detection Using Improved Back-projection Algorithm with Model of Effective Head Permittivity," *Sci. Rep.*, vol. 6, no. February, pp. 1–16, 2016, doi: 10.1038/srep20459.
[35] M. Bocca, A. Luong, N. Patwari, and T. Schmid, "Dial it in: Rotating RF sensors to enhance radio tomography," *2014 11th Annu. IEEE Int. Conf. Sensing, Commun. Networking, SECON 2014*, pp. 600–608, 2014, doi: 10.1109/SAHCN.2014.6990400.
[36] B. Beck, R. Baxley, and X. Ma, "Improving Radio Tomographic Images using multipath signals," pp. 1–4, 2013, doi: 10.1109/icwits.2012.6417789.
[37] V. Rampa, S. Savazzi, M. Nicoli, and M. D'Amico, "Physical Modeling and Performance Bounds for Device-free Localization Systems," *IEEE Signal Process. Lett.*, vol. 22, no. 11, pp. 1864–1868, 2015, doi: 10.1109/LSP.2015.2438176.
[38] V. Rampa, G. G. Gentili, S. Savazzi, and M. D'Amico, "Electromagnetic models for device-free localization applications," *2017 IEEE-APS Top. Conf. Antennas Propag. Wirel. Commun. APWC 2017*, vol. 2017-Janua, pp. 4–7, 2017, doi: 10.1109/APWC.2017.8062225.
[39] S. Zarina, M. Muji, R. Abdul, M. Hafiz, and F. Rahiman, "Optical tomography : Image improvement using mixed projection of parallel and fan beam modes," *Measurement*, vol. 46, no. 6, pp. 1970–1978, 2013, doi: 10.1016/j.measurement.2013.02.011.
[40] S. N. Kane, A. Mishra, and A. K. Dutta, "Optical and X-ray computed tomography scanning of 3D dosimeters," *J. Phys. Conf. Ser.*, vol. 755, no. 1, 2016, doi: 10.1088/1742-6596/755/1/011001.
[41] S. Friedel, "Resolution, stability and efficiency of resistivity tomography estimated from a generalized inverse approach - Friedel - 2003 - Geophysical Journal International - Wiley Online Library," pp. 305–316, 2003, [Online]. Available: http://onlinelibrary.wiley.com/doi/10.1046/j.1365-246X.2003.01890.x/pdf
[42] M. Mallach, P. Gebhardt, and T. Musch, "2D microwave tomography system for imaging of multiphase flows in metal pipes," *Flow Meas. Instrum.*, vol. 53, pp. 80–88, 2017, doi: 10.1016/j.flowmeasinst.2016.04.002.
[43] M. H. F. Rahiman, W. K. T. Thomas, S. J. Soh, and R. A. Rahim, "Microwave Tomography Application and Approaches – A Review," *J. Teknol.*, vol. 3, pp. 133–138, 2015.
[44] M. F. Iskander and Z. Yun, "Propagation Prediction Models for Wireless Communication Systems," *IEEE*

Trans. Microw. Theory Tech., vol. 50, no. 3, pp. 662–673, 2002.

[45] M. Cheney, D. Isaacson, J. C. Newell, S. Simske, and J. Goble, "NOSER: An algorithm for solving the inverse conductivity problem," *Int. J. Imaging Syst. Technol.*, vol. 2, no. 2, pp. 66–75, 1990, doi: 10.1002/ima.1850020203.

[46] Y. Md. Yunos, R. Abd. Rahim, R. G. Green, and M. H. F. Rahiman, "Image Reconstruction Using Iterative Transpose Algorithm for Optical Tomography," *J. Teknol.*, vol. 47, no. 1, 2007, doi: 10.11113/jt.v47.269.

[47] R. C. Conceição, J. J. Mohr, and M. O'Halloran, *An Introduction to Microwave Imaging for Breast Cancer Detection*. 2016. [Online]. Available: http://www.springer.com/series/3740%0Ahttp://link.springer.com/10.1007/978-3-319-27866-7

[48] G. Bindu and S. Semenov, "2D Fused image reconstruction approach for microwave tomography: a theoretical assessment using the FDTD model," *Comput. Methods Biomech. Biomed. Eng. Imaging Vis.*, vol. 1, no. 3, pp. 147–154, Sep. 2013, doi: 10.1080/21681163.2013.776268.

[49] T. Rubæ, P. M. Meaney, P. Meincke, and K. D. Paulsen, "Nonlinear microwave imaging for breast-cancer screening using Gauss-Newton's method and the CGLS inversion algorithm," *IEEE Trans. Antennas Propag.*, vol. 55, no. 8, pp. 2320–2331, 2007, doi: 10.1109/TAP.2007.901993.

[50] A. Voronov, "Regularization in Microwave Tomography for Breast Cancer Imaging Regularization in Microwave Tomography Alexey Voronov," no. December, 2014.

[51] C. Gilmore, "Colin_Gilmore_PhD_Thesis_Final," 2009.

[52] C. S. Wallace and D. M. Boulton, "An information measure for classification," *Comput. J.*, vol. 11, no. 2, pp. 185–194, 1968, doi: 10.1093/comjnl/11.2.185.

[53] M. S. M. Abdullah, M. H. F. Rahiman, N. S. Khalid, and A. S. A. Nasir, "Initial Study of Radio Tomographic Imaging for Human localization by using Simulation Model," J. Phys. Conf. Ser., vol. 2641, p. 8, 2023, doi: 10.1088/1742-6596/2641/1/012019.